

Wide field polarimetry around the Perseus cluster at 350 MHz[★]

M. A. Brentjens

ASTRON, PO Box 2, 7990 AA Dwingeloo, The Netherlands
e-mail: brentjens@astron.nl

Received 1 July 2010 / Accepted 28 October 2010

ABSTRACT

Aims. This paper investigates the fascinating diffuse polarization structures at 350 MHz that have previously been tentatively attributed to the Perseus cluster and, more specifically, tries to find out whether the structures are located at (or near) the Perseus cluster, or in the Milky Way.

Methods. A wide field, eight point Westerbork Synthesis Radio Telescope mosaic of the area around the Perseus cluster was observed in full polarization. The frequency range was 324 to 378 MHz and the resolution of the polarization maps was $2' \times 3'$. The maps were processed using Faraday rotation measure synthesis to counter bandwidth depolarization. The RM-cube covers Faraday depths of -384 to $+381$ rad m^{-2} in steps of 3 rad m^{-2} .

Results. There is emission all over the field at Faraday depths between -50 and $+100$ rad m^{-2} . All previously observed structures were detected. However, no compelling evidence was found supporting association of those structures with either the Perseus cluster or large scale structure formation gas flows in the Perseus-Pisces super cluster. On the contrary, one of the structures is clearly associated with a Galactic depolarization canal at 1.41 GHz. Another large structure in polarized intensity, as well as Faraday depth at a Faraday depth of $+30$ rad m^{-2} , coincides with a dark object in WHAM $H\alpha$ maps at a kinematic distance of 0.5 ± 0.5 kpc. All diffuse polarized emission at 350 MHz towards the Perseus cluster is most likely located within 1 kpc from the Sun. The layers that emit the polarized radiation are less than 40 $\text{pc}/\|B_{\parallel}\|$ thick.

Key words. radio continuum: ISM – galaxies: clusters: individual: Perseus cluster – ISM: magnetic fields – polarization – techniques: polarimetric

1. Introduction

De Bruyn & Brentjens (2005) discovered fascinating structures in sensitive 350 MHz polarimetric observations of the Perseus cluster (Abell 426) with the Westerbork Synthesis Radio Telescope (WSRT). These structures were discovered using a novel data reduction procedure called *RM-synthesis* (Brentjens & de Bruyn 2005), which extends the work of Burn (1966) to multiple lines of sight and arbitrary source spectra, and were tentatively attributed to the Perseus cluster. More information on Faraday depth and depolarization can be found elsewhere in the literature (Tribble 1991; Sokoloff et al. 1998; Vallee 1980).

There were two classes of polarized emission: clearly Galactic, more or less uniform emission at $\phi = 0$ to $+12$ rad m^{-2} , and distinct features that appeared at Faraday depths between $+20$ and $+80$ rad m^{-2} . The second class consisted of two straight features and three other distinct structures. The straight features were the “front” on the western side of the field and the “bar” at the northern edge. A lenticular feature, partially embedded in the front with its major axis parallel to the front, was called the “lens”. Directly east of the lens was a very bright, shell-like object called the “doughnut”. A patch of polarized emission north of the extended tail of NGC 1265 was called the “blob”.

Two possible locations were considered for the second class of emission: our Galaxy, in particular the Perseus arm, and the Perseus cluster itself. We favoured the latter because

- there was a gap in Faraday depth between the large scale Galactic foreground and the distinct features;

- the typical scales in both polarized intensity and Q and U of the features were considerably smaller than the low ϕ emission;
- higher Faraday depths appeared to occur closer to 3C 84;
- the largest structure, the front, was located in the direction of the interface between the Perseus-Pisces super cluster filament and the Perseus cluster;
- a mini survey of 11 polarized point sources within a few degrees of 3C 84 suggested an excess in Faraday depth of $+40$ to $+50$ rad m^{-2} of the emission with respect to these background sources, which was difficult to explain by a small Galactic Faraday rotating cloud.

If the objects indeed resided at or near the cluster, the “front” could be a large scale structure formation shock at the outskirts of the Perseus cluster, squashing a buoyant bubble (the “lens”). It was suggested that the “doughnut” and “blob” are bubbles that were released more recently into the cluster medium by AGN. The discovery of X-ray cavities (Fabian et al. 2003; Clarke et al. 2004) much closer to 3C 84, combined with simulation work on buoyant bubbles and radio relic sources (Enßlin et al. 1998; Enßlin & Gopal-Krishna 2001; Brüggén 2003; Enßlin & Brüggén 2002) reinforced this idea. Highly polarized relic sources have been observed in several galaxy clusters (Röttgering et al. 1997; Enßlin et al. 1998; Govoni et al. 2001, 2005), but never in the Perseus cluster.

A Galactic origin for the high ϕ structures could nevertheless not be ruled out, the main issue being that none of the structures had a counterpart in Stokes I . Because the noise in I is considerably higher than the noise in Q and U due to classical source confusion, a counterpart was only expected for the brightest

[★] Appendix is only available in electronic form at <http://www.aanda.org>

polarized structures. It was nevertheless puzzling that not even the “doughnut” was detected in total intensity, although its polarized surface brightness is only slightly lower than the noise level in Stokes I . One possible explanation is that the Stokes I surface brightness is intrinsically low. This requires a fractional polarization close to the theoretical limit for a synchrotron emitting plasma with an isotropic distribution of the electron velocity vectors ($\approx 70\%$, see e.g. Le Roux 1961; Rybicki & Lightman 1979).

Another explanation is that the Stokes I surface brightness is only *apparently* low. This is a well known property of interferometric observations of Galactic synchrotron emission (Wieringa et al. 1993), which is extremely smooth in Stokes I and is therefore not picked up by the shortest WSRT baseline of $\lesssim 40\lambda$. The Stokes Q and U structure, however, is detectable at much longer baselines due to small scale changes in the observed polarization angle. The apparent fractional polarization can therefore far exceed 100%. This effect could be important in the observations by de Bruyn & Brentjens (2005) because several observing sessions lacked the shortest spacing.

In this paper I present an eight point WSRT mosaic of the region around the Perseus cluster. Faraday rotation measure synthesis was used to map polarized intensity in the area where $2^{\text{h}}58^{\text{m}} \leq \alpha \leq 3^{\text{h}}35^{\text{m}}$ and $39^{\circ}20' \leq \delta \leq 44^{\circ}$ (J2000) for $-384 \leq \phi \leq +381 \text{ rad m}^{-2}$. The primary goal is to assess whether the structures previously observed by de Bruyn & Brentjens (2005) are located near the Perseus cluster or in the Milky Way.

An angular distance of one degree corresponds to 1.5 Mpc at the distance of the Perseus cluster and 35 pc at the distance of the Perseus arm ($\approx 2 \text{ kpc}$). The redshift of the Perseus cluster is $z = 0.0167$ (Struble & Rood 1999). I assume that $H_0 = 72 \pm 2 \text{ km s}^{-1} \text{ Mpc}^{-1}$ (Spergel et al. 2003).

2. Observations

The observations were conducted with the Westerbork Synthesis Radio Telescope (Baars & Hooghoudt 1974; de Bruyn 1996). The array consists of fourteen parallactic 25 m dishes on an east-west baseline and uses earth rotation to fully synthesize the uv-plane in 12 h. There are ten fixed dishes (RT0 – RT9) and four movable telescopes (RTA – RTD).

The distance between two adjacent fixed telescopes is 144 m. The distances between the movable dishes were kept constant (RTA – RTB = RTC – RTD = 72 m, RTB – RTC = 1224 m), while the distance RT9 – RTA was changed for every observing session. The uv-plane is therefore sampled at regular intervals of 12 m out to the longest baseline of 2760 m, lacking only the 0, 12, and 24 m spacings. The regular interval causes an elliptical grating ring with an east-west radius of 4° and a north-south radius of $4^{\circ}/\sin \delta$ at 350 MHz. At this frequency the -5 dB and -10 dB points of the primary beam are at radii of $70'$ and $120'$ respectively. The observations are sensitive to angular scales up to $90'$ at a resolution of $74'' \times 96''$ full width at half maximum (FWHM).

The observations were conducted in mosaic mode. The pointing centres are listed in Table 1. Each session began at a different field to improve the position angle distribution in the uv-plane (see also Table 2). The dwell time per pointing was 150 s and the total integration time after six observing sessions was $8^{\text{h}}22^{\text{m}}$ per field.

The eight frequency bands are each 10 MHz wide and are centred at 319, 328, 337, 346, 355, 365, 374, and 383 MHz. The multi-frequency front ends (Tan 1991) of the WSRT have linearly polarized feeds for this frequency range. The x dipole is

Table 1. Pointing positions of the fields.

Name	α (J2000)	δ (J2000)
A	$3^{\text{h}}06^{\text{m}}24^{\text{s}}$	$42^{\circ}23'$
B	$3^{\text{h}}06^{\text{m}}24^{\text{s}}$	$41^{\circ}07'$
C	$3^{\text{h}}13^{\text{m}}12^{\text{s}}$	$41^{\circ}07'$
D	$3^{\text{h}}13^{\text{m}}12^{\text{s}}$	$42^{\circ}23'$
E	$3^{\text{h}}20^{\text{m}}00^{\text{s}}$	$42^{\circ}23'$
F	$3^{\text{h}}20^{\text{m}}00^{\text{s}}$	$41^{\circ}07'$
G	$3^{\text{h}}26^{\text{m}}48^{\text{s}}$	$41^{\circ}07'$
H	$3^{\text{h}}26^{\text{m}}48^{\text{s}}$	$42^{\circ}23'$

Table 2. Basic information on the six 12 h sessions.

Obs. ID	Obs. start (UTC)	RT9 – RTA (m)	First field
10308301	2003/11/21 16:59:00	48	H
10308473	2003/11/28 16:24:40	60	E
10308694	2003/12/07 15:49:10	36	F
10308727	2003/12/09 15:27:40	72	B
10308798/99	2003/12/13 15:18:50	84	D
10308817	2003/12/15 15:04:10	96	A

oriented east-west, the y dipole north-south. The correlator produced 64 channels in all four cross correlations for each band with an integration time of 10 s. The observations were using 180° front end phase switching. The on-line system applied a Hanning (Harris 1978) lag-to-frequency taper, effectively halving the frequency resolution.

The observations were bracketed by two pairs of calibrators, each consisting of one polarized and one unpolarized source. 3C 345 and 3C 48 were observed before the mosaic and 3C 147 and the eastern hot spot of DA 240 afterwards.

3. Data reduction

Flagging, imaging, and self calibration were performed with the AIPS++ package (McMullin et al. 2004). Flux scale calibration, polarization calibration, ionospheric Faraday rotation corrections, and deconvolution were performed with a calibration package written by the author and based on the table, measures, and fitting modules of AIPS++/CASA. Channels and frequency bands are numbered from 1.

3.1. Data quality

Although the lowest and highest sub bands had to be discarded, the data quality was generally good and interference levels were low. The Sun was still up at the beginning of all but the first observing sessions (see Table 2). The system temperatures were usually between 130 K and 220 K with the median at 175 K. The expected thermal rms image noise in a clean Hanning tapered channel after $8^{\text{h}}22^{\text{m}}$ of integration is $2.6 \text{ mJy beam}^{-1}$ (Thompson et al. 1998).

Because of the Hanning tapering, I processed only the odd numbered channels from 5 to 59 inclusive. Approximately 20% of the data in these channels were flagged, hence the expected thermal rms image noise per field at full resolution is $0.22 \text{ mJy beam}^{-1}$ after averaging all processed channel maps from the six usable spectral windows. The visibilities were time averaged to 30 s before calibration and imaging to reduce processing time.

3.2. Calibration

The flux scale, bandpass, and polarization leakages were calibrated simultaneously per individual channel by solving the Hamaker-Bregman-Sault Measurement Equation (Sault et al. 1996) for the unpolarized calibrator sources 3C 147 and 3C 48. The Perley & Taylor (1999) calibrator fluxes, which extend the Baars et al. (1977) flux scale to lower frequencies¹, established the absolute flux scale.

The polarization leakages were solved per channel because of their strong 17 MHz semi-periodic frequency dependence (see e.g. de Bruyn & Brentjens 2005). The diagonal phases of the RT0 Jones matrix were fixed at 0 rad. The remaining $x - y$ phase difference was determined using the polarized sources.

The ionospheric Faraday rotation was corrected with the method from Brentjens (2008). All fields were subsequently individually self calibrated (Pearson & Readhead 1984) with a CLEAN component (Högbom 1974) based sky model in I and Q . The strongly frequency dependent polarization leakages required a separate CLEAN model per channel.

Fields A and B were calibrated with three phase-only iterations because the total flux in these fields was too low for amplitude self calibration. The remaining fields were calibrated with two phase-only iterations and one amplitude/phase iteration. Each 10 MHz band was self calibrated with a single Jones matrix per antenna at 30 s intervals.

3.3. Imaging

All fields were imaged and deconvolved separately. The point spread functions (PSFs) and dirty channel images in all Stokes parameters were created using AIPS++. The uv -plane was uniformly weighted. Because of a fractional bandwidth of 15%, the maps had to be convolved to a common resolution of $74'' \times 96''$ FWHM, elongated north-south, using a Gaussian uv -plane taper. All maps are in north celestial pole (NCP) projection with the projection centre at 3C 84 (J2000: $\alpha = 3^{\text{h}}19^{\text{m}}48^{\text{s}}.1601$, $\delta = +41^{\circ}30'42''.106$). The dirty maps have 2048×2048 pixels of $30'' \times 30''$ each.

The central 1024×1024 pixels of the dirty images were deconvolved using a Högbom CLEAN (Högbom 1974). The CLEAN mask consisted of all Stokes I pixels brighter than 6, 5, 10, 10, 15, 8, 10, and 10 mJy beam⁻¹ for fields A – H, respectively. The deconvolution was stopped whenever the maximum residual in the masked area was below 0.5 mJy beam⁻¹ or when 10 000 iterations were completed without reaching the threshold. The resulting model images were convolved with a $74'' \times 96''$ FWHM elliptical Gaussian and added back to the residual images. The deconvolution of the Q and U images was terminated after 10 000 iterations or if a threshold of 0.5 mJy beam⁻¹ was reached.

The primary beam corrected images were combined into one mosaic image per channel per Stokes parameter. The restored Stokes Q and U mosaic maps were subsequently convolved to a resolution of $2'.0 \times 3'.0$ FWHM to enhance the signal to noise ratio of extended emission. The expected rms thermal noise after averaging all low resolution images for one field is increased to 0.4 mJy beam⁻¹ near the pointing centres and 0.3 mJy beam⁻¹ in

¹ The flux scale of WSRT observations has since 1985 been based on a 325 MHz flux of 26.93 Jy for 3C 286 (the Baars et al. 1977, value). On that flux scale, the 325 MHz flux of 3C 295 is 64.5 Jy, which is almost 7% more than the value assumed at the VLA and in this paper (de Bruyn, priv. comm.).

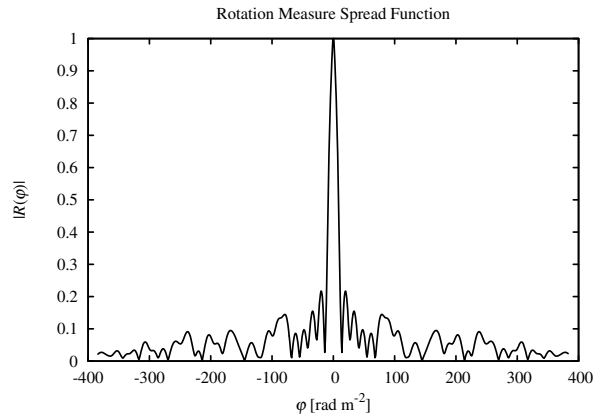


Fig. 1. Absolute value of the RMSF corresponding to the frequency coverage of the observations. The FWHM of the main peak is 16.4 rad m^{-2} .

the areas surrounded by four pointings because the convolution suppresses data from long baselines.

Although the theoretical Q and U noise is approached at the intersection of fields A, B, C, and D, the RMS image noise in most areas of the mosaic is a factor of two higher due to Stokes U dynamic range problems associated with 3C 84.

3.4. RM-synthesis

The 143 good quality polarization maps were processed using RM-synthesis (Brentjens & de Bruyn 2005) to avoid bandwidth depolarization. The RM-cube covers the range $-384 \leq \phi \leq +381 \text{ rad m}^{-2}$ in steps of 3 rad m^{-2} . The absolute value of the corresponding RMSF is displayed in Fig. 1. The FWHM of the main peak is 16.4 rad m^{-2} and the side lobes are of the order of 15%–20%, requiring deconvolution in ϕ -space using an RM-CLEAN² similar to the work of Heald et al. (2009).

4. Images

The size of the mosaic is $4'.5$ in declination by $7'$ in right ascension. Figure 2 shows a full resolution Stokes I map of the area. It is the average of 143 channels with an average frequency of 351 MHz. The peak flux is $19.97 \text{ Jy beam}^{-1}$ at the location of 3C 84. The actual RMS noise level of the total intensity map ranges from $1.5 \text{ mJy beam}^{-1}$ in the most western fields, A and B, to 3 mJy beam^{-1} in field G. The difference between the expected thermal noise and the observed rms noise is caused by ionospheric non-isoplanaticity. It is worse in the eastern fields because they contain more bright sources than the western fields. These problems are unpolarized and therefore do not limit the dynamic range of the Stokes Q and U images. The total dynamic

² This type of deconvolution works well if there is only one component along the line of sight, or if the emitting regions are separated in ϕ by more than the width of the rmsf. There may be systematic errors in the Faraday depth of each individual component up to the width of the rmsf if the components are closer together and of similar brightness (Rudnick, priv. commun.). This is effectively an interference effect due to the complex nature of the rmsf. The effect can potentially increase the scatter in ϕ , but will average out over sufficiently many lines of sight. Although it is unimportant for the conclusions drawn in the remainder of this paper, it is something to take into account when doing RM work above 1 GHz, because the rmsf in such observations is typically very wide.

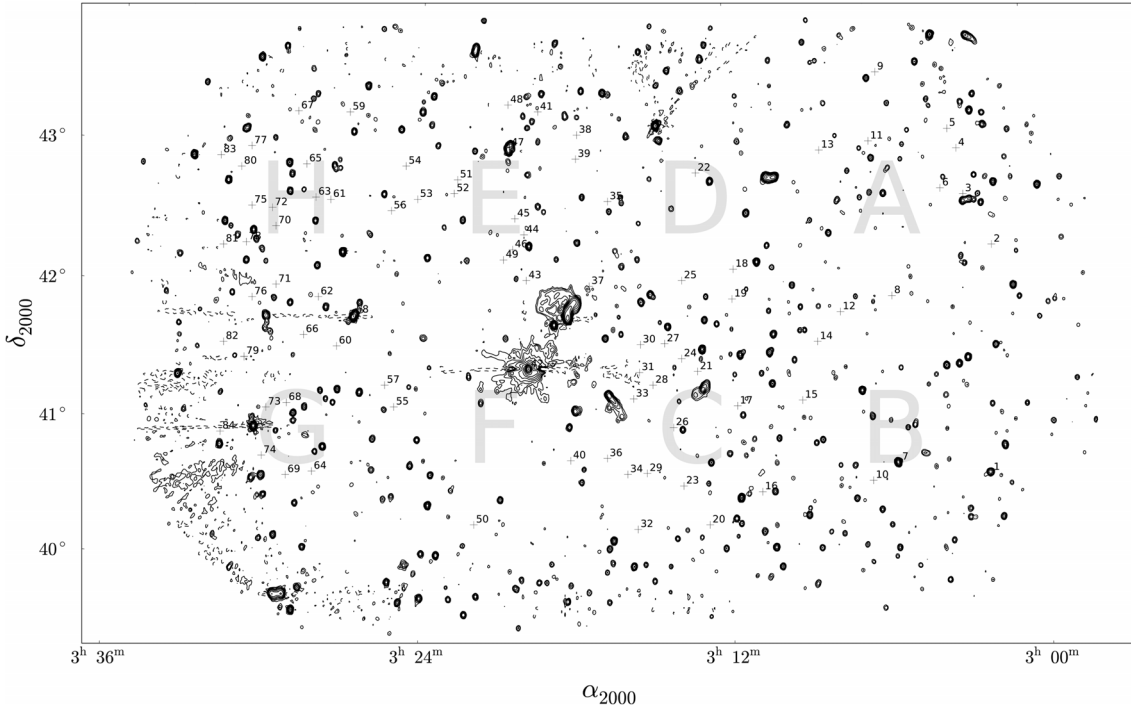


Fig. 2. Overview of the mosaic in total intensity at a resolution of $74'' \times 96''$ FWHM. The contours are drawn at $-9, +9, 18, 36$ mJy beam $^{-1}$... 18 Jy beam $^{-1}$. The numbered crosses mark the locations of the Faraday spectra in Fig. 3. The dynamic range in this map is approximately 6000:1.

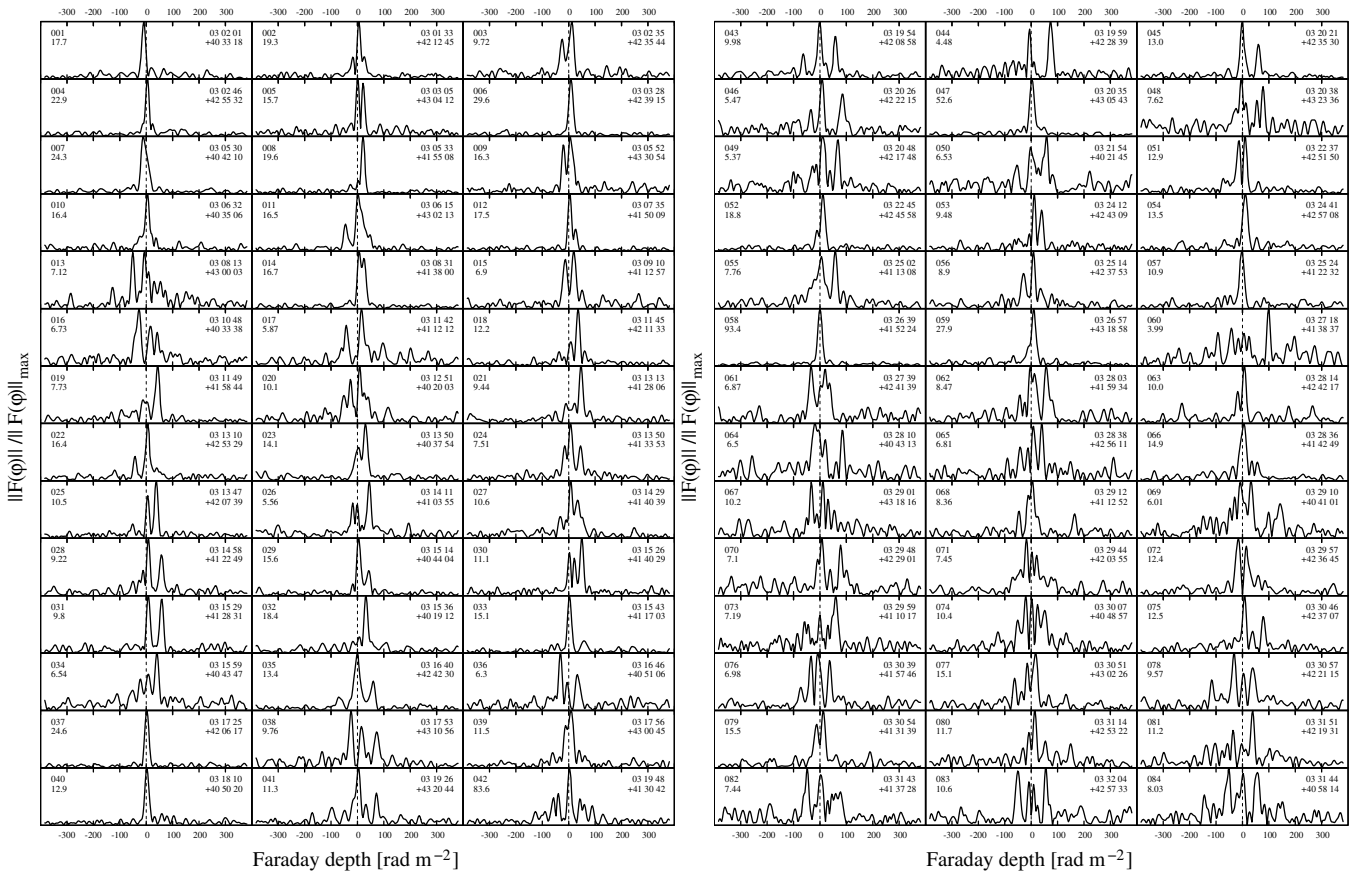


Fig. 3. Faraday dispersion spectra of interesting lines of sight through the mosaic. The *top left* number is the label of the spectrum in Fig. 2. The vertical scale is different for each graph. The peak brightness in mJy beam $^{-1}$ rms $^{-1}$ is displayed below the number of the spectrum. The *top right corner* of each plot lists the J2000 α and δ .

range is approximately 6000:1. The labelled crosses indicate the positions of the Faraday dispersion spectra presented in Fig. 3. There is no significant Stokes I source at most of these locations.

The individual Faraday dispersion spectra (hereafter simply spectra) in Fig. 3 show that emission at multiple Faraday depths along the same line of sight are the norm, rather than the exception in this part of the sky. The Faraday depth of significant emission ranges from -60 rad m^{-2} (spectrum 43) to $+100 \text{ rad m}^{-2}$ (spectrum 60), or perhaps $+140 \text{ rad m}^{-2}$ if the complexity in spectrum 69 is real. Spectra 1, 6, and 37 show the quality of the RM-CLEAN: all have residuals of less than 2% of the main peak, which is comparable to the rms noise of nearby pixels.

Spectra 24, 28, and 31 are lines of sight through the “lens” structure. They all show clear peaks at a Faraday depth of approximately $+50 \text{ rad m}^{-2}$, in addition to peaks near $+6 \text{ rad m}^{-2}$. Spectrum 30 goes through the centre of the “doughnut” and is triple valued. Spectrum 43 goes straight through the “blob” directly north of the extended tail of NGC 1265. The most complex spectra are located in the fields G and H. The highest absolute Faraday depths occur in fields E, G, and H.

Figure A.1 shows the most interesting part of the RM-cube. The first few frames are devoid of significant emission. The arc between -72 and -60 rad m^{-2} is instrumental and is caused by a minor calibration error of unknown origin in Stokes U of field G. The first significant emission appears at a Faraday depth of -48 rad m^{-2} in the northern four fields, especially in fields A (north-west) and H (north-east). The patches have structure at scales of a few arc minutes. The emission increases particularly in the north-eastern part of the mosaic when the Faraday depth approaches 0 rad m^{-2} .

The entire mosaic is filled with emission with structure at typical scales of tens of arc minutes at Faraday depths between -6 and $+12 \text{ rad m}^{-2}$. The peak brightness is almost $30 \text{ mJy beam}^{-1} \text{ rms}^{-1}$ in the north-west corner. This type of emission dissolves at $\phi \approx +18 \text{ rad m}^{-2}$. At that point, a well-defined linear structure develops between $\alpha \approx 3^{\text{h}}12^{\text{m}}$, $\delta \approx +39^{\circ}7$ and the north-west corner of the mosaic. The following frames show that the emission slowly moves east with increasing Faraday depth. It also becomes less uniform. The thin straight line that runs from $\alpha = 3^{\text{h}}16^{\text{m}}$, $\delta \approx +40^{\circ}$ to $\alpha = 3^{\text{h}}6^{\text{m}}$, $\delta \approx +43^{\circ}5$ at $\phi = +42 \text{ rad m}^{-2}$ is called the “front” in de Bruyn & Brentjens (2005). There are several highly significant structures in the area between $\alpha \approx 3^{\text{h}}8^{\text{m}} - \alpha \approx 3^{\text{h}}8^{\text{m}}$, $\delta \approx +41^{\circ}5$ and the northern edge of the mosaic. There are also small patches of emission across the rest of the map, particularly in the north-eastern area.

The “doughnut” and brightest parts of the “lens” (de Bruyn & Brentjens 2005) are visible at Faraday depths of $+48$ and $+54 \text{ rad m}^{-2}$, along with several patches north of them. There is a blob of emission at $\phi = +60 \text{ rad m}^{-2}$ around line of sight 43, north of 3C 84 and directly north of the extended tail of NGC 1265. The “bar” (de Bruyn & Brentjens 2005) is visible around line of sight 44 at a Faraday depth of $+78 \text{ rad m}^{-2}$. There are still several significant patches of polarized emission in fields E and H, which fade away at Faraday depths above 100 rad m^{-2} .

5. Discussion

The bright emission that spans the entire mosaic at a relatively uniform Faraday depth of 0 to $+12 \text{ rad m}^{-2}$ is evidently Galactic: its spatial structure, Faraday depth, and brightness temperature are typical for medium latitudes and comparable resolutions (Uyaniker et al. 1999; Haverkorn et al. 2003a,b; Schnitzeler et al. 2007). The brightness temperature of the polarized intensity is 5

to 10 K with a maximum of 14 K^3 . The Faraday depth range is consistent with observations by Haverkorn et al. (2003a) at similar l and $|b|$.

In the remainder of this section I argue that most, if not all, of the other extended polarized emission at both higher and lower Faraday depths is Galactic and is not associated with the Perseus cluster. I will do that by discussing the arguments mentioned in the introduction in the light of the new observations.

5.1. A special Faraday depth

In Fig. 3, spectra 24, 28, and 31 clearly show the separation between the emission at low ϕ and the “front” and the “doughnut”. It is also evident in spectrum 43 (the “blob”) and spectra 44, 46, and 49 (the “bar”). However, as can be seen in the images in Fig. A.1 and the Faraday dispersion spectra in Fig. 3, there is significant emission at *all* Faraday depths between -48 rad m^{-2} and $+100 \text{ rad m}^{-2}$.

The strong emission at $\phi = +6 \text{ rad m}^{-2}$ connects smoothly to the emission at higher Faraday depth at $\phi = +18 \text{ rad m}^{-2}$ in fields A and B. Spectrum 55 contains emission at $\phi = +60 \text{ rad m}^{-2}$. Several spectra to its east contain emission between $+50 \text{ rad m}^{-2}$ and $+100 \text{ rad m}^{-2}$ (spectrum 60). See for example the patches between lines of sight 60, 82, 75, and 61 at $\phi = +84 \text{ rad m}^{-2}$.

When considering the entire mosaic, there is no trend of higher Faraday depths closer to 3C 84. Of course there is a west to east gradient between $\phi = +18 \text{ rad m}^{-2}$ and $\phi = +60 \text{ rad m}^{-2}$, but higher and lower Faraday depths occur throughout the mosaic. The highest absolute Faraday depths and most complex Faraday dispersion spectra occur in fields E, G, and H in areas that can not be associated with the Perseus cluster.

The Faraday depths of the “front” ($+42$ to $+48 \text{ rad m}^{-2}$), “lens” ($\approx +50 \text{ rad m}^{-2}$), “doughnut” ($\approx +50 \text{ rad m}^{-2}$), “blob” ($+60 \text{ rad m}^{-2}$), and “bar” ($+78 \text{ rad m}^{-2}$) are neither extreme, nor special when compared to the range of Faraday depths observed in this mosaic. One can therefore not distinguish between Galactic polarized emission and cluster related polarized emission in this field based solely on the value of the Faraday depth if it is in the range from -48 rad m^{-2} to $+100 \text{ rad m}^{-2}$.

5.2. Smaller spatial scales at high $|\phi|$

Figures 4 and 5 show the position angle of the electric field on top of polarized intensity contours. The position angles have *not* been derotated to 0 wavelength because the 1σ uncertainty of the Faraday depth at $\phi > +18 \text{ rad m}^{-2}$ was generally worse than 0.5 rad m^{-2} . Instead, the vectors reflect the position angles at $\lambda_0^2 = 0.73275 \text{ m}^{-2}$ (350.22 MHz), hence no conclusions can be drawn from the absolute position angles in the images. The images are only used to estimate typical scales at which the position angle changes by a radian or more at 350.22 MHz.

The area of the “lens”, “doughnut”, and “blob” at $\phi = +51 \text{ rad m}^{-2}$ is shown in Fig. 4. The lens is difficult to recognize due to the lower signal to noise ratio compared to the observations by de Bruyn & Brentjens (2005). The position angles are fairly uniform in patches of the order of $15'$ across, changing abruptly at the borders between these patches. The polarized patches at the same Faraday depth in field D, north of the “lens”, “doughnut”, and “blob”, are comparable, but are too far away

³ At 351 MHz, 10 mJy beam^{-1} of $2' \times 3'$ FWHM corresponds to a brightness temperature of 4.6 K .

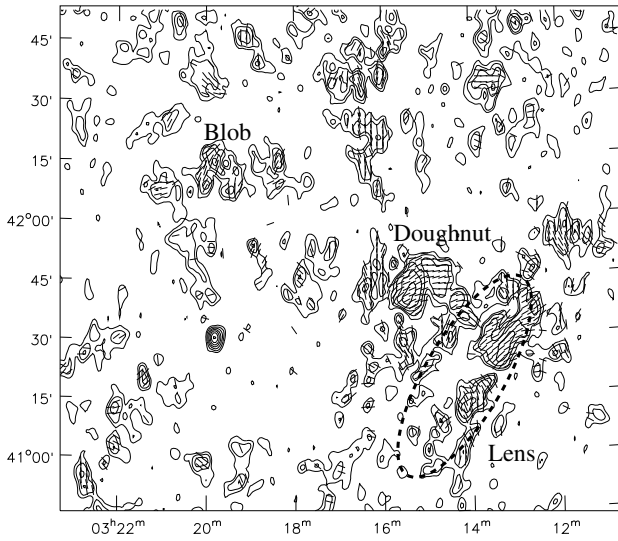


Fig. 4. Polarization vectors at 350.22 MHz overlaid on contours of $|F(\phi)|$ at $\phi = +51 \text{ rad m}^{-2}$ of the “doughnut” area. The contours start at $2.5 \text{ mJy beam}^{-1} \text{ rmsf}^{-1}$ and are scaled by a factor of $\sqrt{2}$.

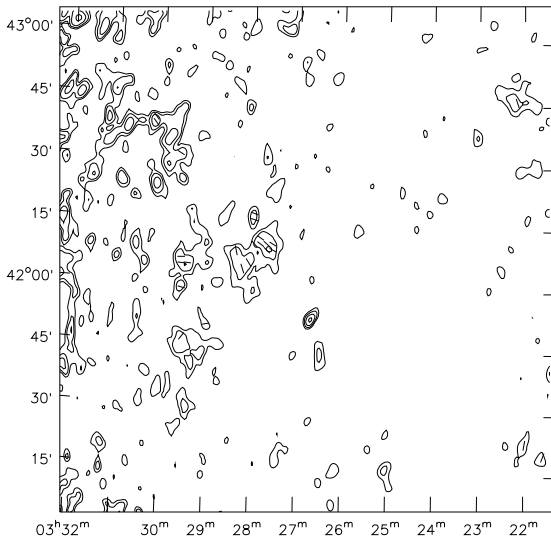


Fig. 5. Polarization vectors at 350.22 MHz overlaid on contours of $|F(\phi)|$ at $\phi = +84 \text{ rad m}^{-2}$ of the intersection of fields G and H. The contours start at $2.5 \text{ mJy beam}^{-1} \text{ rmsf}^{-1}$ and are scaled by a factor of $\sqrt{2}$.

from 3C 84 to be associated with the Perseus cluster. The polarized emission in fields G and H at $\phi = +84 \text{ rad m}^{-2}$ has fairly uniform polarization angles across each emission patch. These patches are $3' \text{ to } 10' \times 20'$ large (see Fig. 5).

The polarization angle structure of a few representative images from the full RM-cube is shown in Fig. A.2. At $\phi = +6 \text{ rad m}^{-2}$ the position angles are fairly uniform at scales of $30'$ to $90'$. At $\phi = +30 \text{ rad m}^{-2}$ it changes at $20'$ to $30'$ scales. At $\phi = +42 \text{ rad m}^{-2}$ the typical scale is $10'$ to $30'$, and at higher Faraday depths scales range from $3'$ to $20'$. These changes can be due to differences in intrinsic polarization, changes in Faraday rotation, or a combination of the two effects. Because of the uncertainty of the precise Faraday depth, it is not possible to discriminate between these possibilities.

The scale size at which the polarization angles change *does* decrease with increasing $|\phi|$, but this is not limited to the area near 3C 84 and is therefore no argument in favour of nor against cluster association. Furthermore, the scales at which the polarization angles at 350.22 MHz change in the “lens”, “doughnut”, “front”, and “blob” are comparable to other structures at similar Faraday depth that can not be linked to the Perseus cluster.

5.3. Fractional polarization

The fractional polarization at 351 MHz was estimated by dividing the polarized intensity, integrated over all Faraday depths, by the 408 MHz Haslam et al. (1982) total intensity map converted to 351 MHz using a Galactic synchrotron brightness temperature spectral index $\beta = -2.8$ (Reich & Reich 1988b,a; Platania et al. 1998). Between 10 MHz and 100 MHz, the spectral index is -2.55 (Cane 1979), hence the actual spectral index between 408 MHz and 351 MHz is probably closer to -2.7 . The difference with -2.8 is negligible for the small extrapolation from 408 MHz to 351 MHz.

The noise in the derotated Q and U maps is Gaussian:

$$\mathcal{P}(n) dn = \frac{1}{\sigma \sqrt{2\pi}} e^{-\frac{(n-\mu)^2}{2\sigma^2}} dn, \quad (1)$$

where $\mathcal{P}(n) dn$ is the probability of finding a noise value between n and $n + dn$, and μ and σ are the mean and standard deviation. If the Q and U noise distributions have equal σ , zero mean, and are uncorrelated, then the probability of finding a noise value of $|F|$ between f and $f + df$ is:

$$\mathcal{P}(f) df = \begin{cases} \frac{f}{\sigma^2} e^{-\frac{f^2}{2\sigma^2}} df & \text{if } f \geq 0 \\ 0 & \text{if } f < 0. \end{cases} \quad (2)$$

The rms of $|F|$ is equal to the rms of Q and U , which is $\sigma\sqrt{2}$. The mean value of the noise in $|F|$ is

$$\langle f \rangle = \sigma \sqrt{\frac{\pi}{2}}. \quad (3)$$

The polarized surface brightness of a low S/N line of sight, integrated over a range of equidistant Faraday depths $\phi_1 \dots \phi_n$, and corrected for the non-zero mean of the noise level, is therefore

$$|P| = B^{-1} \sum_{i=1}^n \left(|F(\phi_i)| - \sigma \sqrt{\frac{\pi}{2}} \right), \quad (4)$$

where B is the area under the restoring beam of the RM-CLEAN divided by $\Delta\phi = |\phi_{i+1} - \phi_i|$. See Wardle & Kronberg (1974) for a more general treatment of uncertainties and biases in RM work.

Wolleben et al. (2006) have conducted an absolutely calibrated survey of polarized emission north of declination -30° at 1.41 GHz with the 26 m telescope at the DRAO site at a resolution of $36' \text{ FWHM}$. The integrated 351 MHz polarized intensity overlaid with the polarized intensity contours from Wolleben et al. (2006) is shown in Fig. 6. The noise level in the 351 MHz map is approximately 0.5 K. With a spectral index of -2.8 , the brightness temperature at 351 MHz should be 50 times higher than at 1.41 GHz. This is approximately the case in most of the field, which implies that there is very little depolarization between 1.41 GHz and 351 MHz. In some places, the polarized intensity is even higher at 351 MHz than one would expect based on the low resolution polarized intensity at 1.41 GHz and a spectral index of -2.8 . Examples are the area containing the

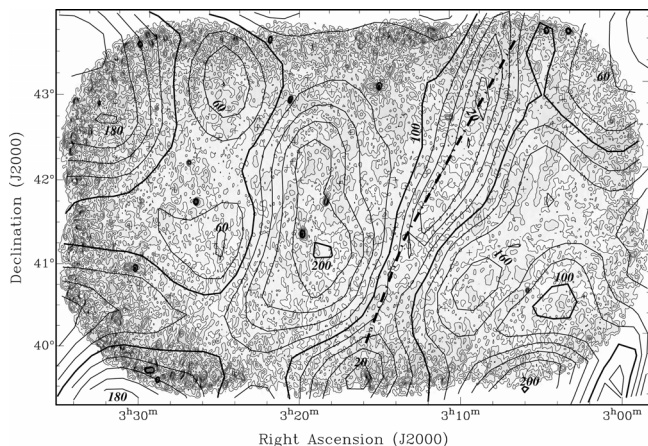


Fig. 6. Wolleben et al. (2006) polarized intensity contours at 1.41 GHz overlaid on the integrated polarized intensity map of the RM-cube. The thin contours represent the polarized intensity at 351 MHz and are drawn at 4 to 40 K in steps of 4 K. The thick contours represent the Wolleben map and are drawn at 20 to 200 mK in steps of 20 mK. The dashed line represents the “front”.

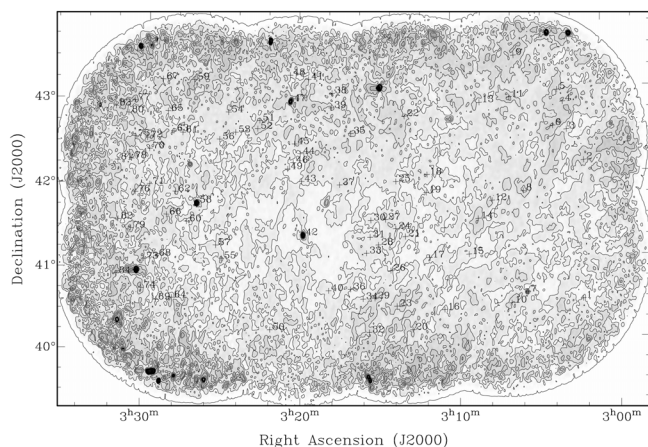


Fig. 7. Map of the fractional polarization at 351 MHz. The contours are 10%, 20%, 30%, 40%, and 50%. The grey scale runs linearly from 0% (white) to 70% (black).

“front”, “lens”, and “doughnut”, and the highly polarized region in field A. This is probably caused by beam depolarization in the Wolleben et al. (2006) observations due to differences in intrinsic polarization angle at scales well below 36′ that are resolved in the observations presented here.

Figure 7 displays the fractional polarization. It is mostly between 10% and 20% with a maximum of 35% in field A. Although these values are well below the theoretical maximum of 70%, they are relatively high. The low fractional polarization between 3C 84 and NGC 1265 is an artifact caused by the low resolution (0.85) of the Haslam et al. (1982) map, which blends these powerful sources. Because there are no absolutely calibrated polarimetric single dish observations of the field near 351 MHz, my maps may lack Q and U features at scales $\geq 90'$. The fractions are therefore strictly speaking lower limits.

The lack of depolarization implies that the synchrotron emitting areas have a Faraday thickness of less than 1 rad m^{-2} . This is remarkable because the range of Faraday depths is two orders of magnitude larger. Assuming a line of sight magnetic field of $1 \mu\text{G}$ and a local electron density of 0.03 cm^{-3} (Gómez et al. 2001; Cordes & Lazio 2002), a Faraday thickness of 1 rad m^{-2} corresponds to only 40 pc, which is difficult to reconcile with

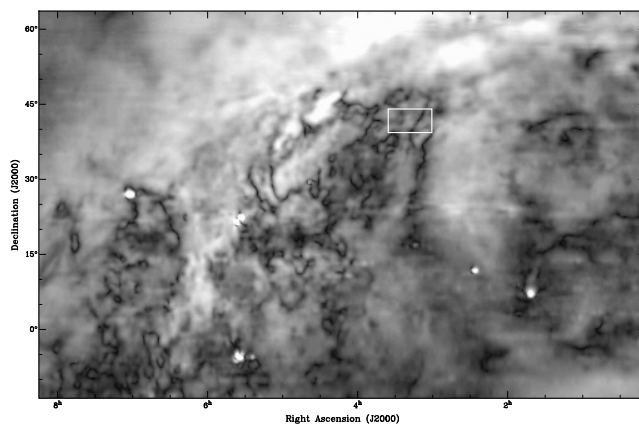


Fig. 8. Part of the Wolleben et al. (2006) polarized intensity map at 1.4 GHz. The position and extent of the Perseus mosaic is indicated by the white rectangle. The grey scale is proportional to the square root of the polarized intensity and runs from 0 (black) to 500 mK (white).

the smoothness of the Galactic synchrotron foreground unless the structures are close to the Sun. Assuming that the emitting patches are approximately as thick as they are wide, non-detection of Stokes I at 90′ scales implies that the clouds are closer than 1.6 kpc. Polarization observations at lower frequencies are required to follow the depolarization and determine the exact Faraday thickness.

5.4. The “front” and the Perseus-Pisces super cluster

The “front” was tentatively interpreted by de Bruyn & Brentjens (2005) as a large scale structure formation shock at the interface between the Perseus cluster and the Perseus-Pisces super cluster. It was unclear at that time whether the “front” extended much beyond the primary beam of the WSRT. As can be seen in the image at $\phi = +42 \text{ rad m}^{-2}$ in Fig. A.1, it does. The location of the “front” is indicated by the dashed line in Fig. 6. It runs from line of sight 32 via lines of sight 18 and 12 to line of sight 19. Association with the Perseus cluster is therefore unlikely.

As can be seen in the 21 cm polarization map by Wolleben et al. (2006) (Fig. 8), the Perseus cluster is located behind the north-western tip of a large field of Galactic depolarization canals (see e.g. Fletcher & Shukurov 2006 and Haverkorn et al. 2000, for an in-depth treatment of depolarization canals). Interestingly, the “front” coincides with the centre of such a canal, hence the “front” is very likely Galactic. If the “lens” is associated with the “front”, it must also be Galactic. The two structures may of course be unrelated, but their coincidence in Faraday depth, position, and position angle suggests otherwise.

5.5. ϕ with respect to background sources

The excess of $+40$ to $+50 \text{ rad m}^{-2}$ in ϕ of the structures observed by de Bruyn & Brentjens (2005) with respect to the background sources was based on a small number of polarized sources near the centre of the mosaic. Taylor et al. (2009) have since published a comprehensive RM catalogue based on a re-analysis of 37 543 NVSS sources, allowing a more detailed analysis. de Bruyn et al. (in prep.) have also conducted WSRT observations of more than 200 polarized sources in and around this area during the 2004/2005 winter season. Those data will be reported in a subsequent paper.

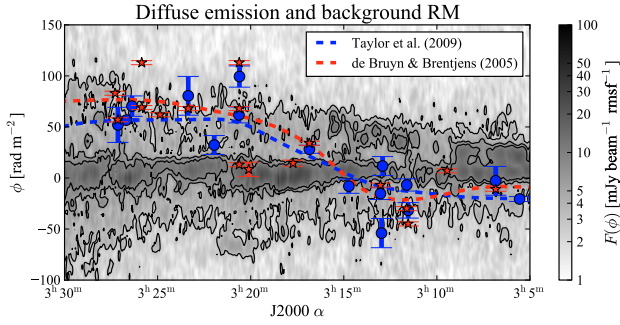


Fig. 9. Diffuse emission with respect to background RM. The grey scale image is the logarithm of the maximum brightness in a 1 degree wide slab. The background sources are from a 4 degree wide slab. Both slabs are centred at $\delta = 41^{\circ}48'12''$. Contour levels are at 3, 6, and 9 mJy beam $^{-1}$ rmsf $^{-1}$.

Figure 9 illustrates the relation between the Taylor et al. (2009) sources, the de Bruyn & Brentjens (2005) sources, and the diffuse polarized emission. The logarithmic grey scale image represents the *maximum* $|F(\phi)|$ at a particular Faraday depth and horizontal position in a 1° thick horizontal slab through the RM-cube, centred at $\alpha = 3^{\text{h}}20^{\text{m}}$ and $\delta = +41^{\circ}48'12''$. The Taylor et al. (2009) sources are those within a 4° thick horizontal slab centred at the same position. The sources from de Bruyn & Brentjens (2005) partly overlap with the Taylor et al. (2009) selection. Where they do, the rotation measures agree within the error bars. The α tick marks indicate the right ascension at the centre of the slabs. The dashed lines are the background points convolved with a Gaussian kernel of $\Delta\alpha = 5^{\text{m}}$ FWHM.

Both dashed curves show a clear trend in the background RM. The same trend is visible in the polarized emission at $\phi > +12$ and $\alpha < 3^{\text{h}}17^{\text{m}}$. This suggests that there is an area behind the emission at high ϕ with a relatively uniform Faraday thickness of -45 ± 5 rad m $^{-2}$. The fact that the excess extends to the westernmost edge of the image rules out a cluster origin.

The scatter in background RMs is relatively large, as is the scatter in the Faraday depth of polarized emission. Whether this scatter can be explained adequately by a turbulent magnetized ISM or by the IGM around the background sources needs to be investigated using numerical MHD simulations.

5.6. A crude model

The large scale magnetic field in the vicinity of the Sun is estimated at $1.4 \mu\text{G}$ and points towards $l \approx 80^{\circ}$ (Han & Qiao 1994; Sun et al. 2008). The Faraday depth at $l \approx 150^{\circ}$ should therefore be slightly negative, which is clearly not observed. The most prominent polarized features are instead observed at positive Faraday depth, indicating a magnetic anomaly in the direction of the Perseus cluster.

It is interesting to briefly explore the conditions in the ISM that are required to explain the observed Faraday depths. Figure 10 illustrates the emerging picture. Because of the generally high degree of polarization and lack of depolarization between L band and 350 MHz, it is likely that the areas with the most pronounced polarized emission are less than 40 pc thick.

The wide spread emission at $\phi \approx +6$ rad m $^{-2}$ is probably the most nearby component because of its uniform Faraday depth and polarization angle structure at large spatial scales. The uniform Faraday depth also suggests that $n_e B_{\parallel}$ towards the Perseus

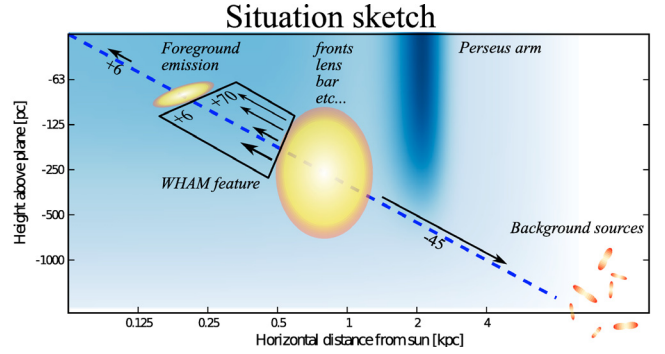


Fig. 10. Sketch of the possible layout of emission and magnetic fields in the observed field. Solid arrows indicate orientation and strength of B_{\parallel} . Yellow indicates synchrotron emission and blue the thermal electron density. The image is a vertical slice through the southern half of the Milky Way at $l = 150^{\circ}$. The dashed line is the line of sight towards the Perseus cluster at $b = -13^{\circ}$.

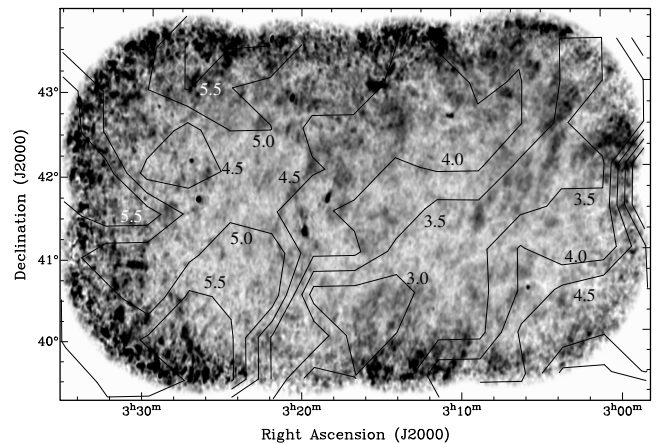


Fig. 11. Integrated polarized intensity at 351 MHz overlaid with WHAM H α surface brightness contours in Rayleighs. The grey scale runs from 0 (white) to 40 mJy beam $^{-1}$ (black). The resolution of the polarized intensity map is $2' \times 3'$ FWHM.

cluster near the Sun is rather uniform. The thickness of this Faraday rotating layer is therefore

$$d_{+6} \approx 250 \left[\frac{0.03 \text{ cm}^{-3} \times 1 \mu\text{G}}{\langle n_e B_{\parallel} \rangle} \right] \text{ pc.} \quad (5)$$

If the polarized emission at $\phi = +6$ rad m $^{-2}$ is located closely behind this area, this would place the emission near the edge of the local bubble, which is estimated to have a radius of approximately 200 pc (see e.g. Sun et al. 2008). This is consistent with the suggestion by Wolleben et al. (2006) that the Sun resides inside a synchrotron emitting region, provided that the emission lies beyond a non-emitting magnetized plasma.

Beyond this emission follows an area with a Faraday thickness of approximately $+6$ in the west to $+70$ rad m $^{-2}$ at the centre of the mosaic, as was discussed in the previous section. This layer is followed by the emission containing the western diagonal structures and the “front”, “lens”, “doughnut”, and “bar” near the centre of the mosaic. The diagonal features in this area – including the “front” and “lens” – appear connected spatially as well as in Faraday depth.

Figure 11 shows the integrated H α surface brightness contours observed by the Wisconsin H α Mapper (WHAM, Haffner et al. 2003) overlaid on the integrated polarized intensity map. There is an absorption feature in the integrated H α map running

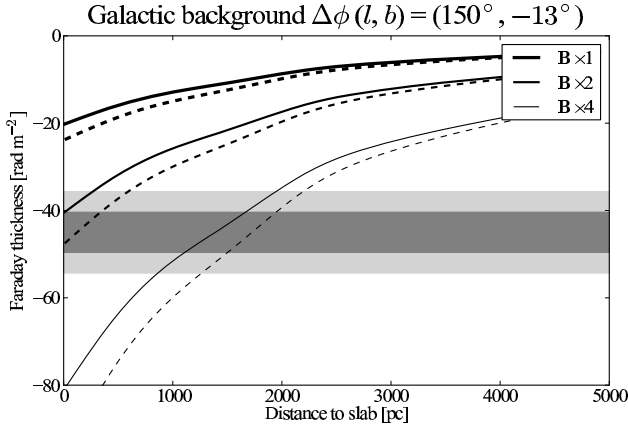


Fig. 12. Model Faraday thickness of a slab along the line of sight towards the Perseus cluster as a function of the distance to the near side of the slab. The far side of the slab is held constant at 20 kpc distance from the Sun. The assumed magnetic pitch angle is 12° (solid lines) or 8° (dashed lines). The thinner sets of lines represent magnetic models where the total field strength was multiplied with a factor of two or four. The grey bar indicates the 1σ and 2σ uncertainty levels of the observed Faraday thickness of the slab between the high- ϕ polarized emission and the polarized background sources.

from the centre of the southern edge of the field to the north-west corner. The minimum $H\alpha$ brightness coincides with the bright, complex polarized patch around line of sight 32 that is visible between $\phi = -24 \text{ rad m}^{-2}$ and $+36 \text{ rad m}^{-2}$. Furthermore, the $60 \mu\text{m}$ and $100 \mu\text{m}$ IRAS (Neugebauer et al. 1984) infrared maps show enhanced infrared emission here, as well as diagonally towards the north west. The centre of the dark $H\alpha$ feature runs along the diagonal structures in the western part of the field between $\phi = +24 \text{ rad m}^{-2}$ and $\phi = +36 \text{ rad m}^{-2}$. The WHAM feature is visible between -20 and $+20 \text{ km s}^{-1}$, but is most prominent between -20 and 0 km s^{-1} . Assuming a central velocity of $-5 \pm 5 \text{ km s}^{-1}$ and a Galactic rotational velocity near the Sun of $200 \pm 10 \text{ km s}^{-1}$ (Merrifield 1992; Binney & Dehnen 1997), the kinematic distance to the cloud is $0.5 \pm 0.5 \text{ kpc}$. The polarized emission at high Faraday depth is probably located behind the WHAM structure.

Another hint at the proximity of the high- ϕ emission comes from the $-45 \pm 5 \text{ rad m}^{-2}$ offset in Faraday depth between the high- ϕ emission and the polarized background sources. Assuming that most of this offset is due to the Milky Way, one can estimate the Faraday thickness of this layer using models for the electron density and magnetic field along the line of sight, and a lower and upper integration limit. The electron model consists of the NE2001 spiral arms, thin disc, and thick disc (Cordes & Lazio 2002) modified according to Gaensler et al. (2008). The magnetic field model is the ASS+ring model from Sun et al. (2008). The upper integration limit was set at 20 kpc from the Sun. Simulations were performed with magnetic pitch angles of 12° (Sun et al. 2008) and 8° (Han & Qiao 1994) and with different total field strengths (once, twice, and four times the strength from Sun et al. 2008). The results are shown in Fig. 12.

The points where the curves intersect with $\Delta\phi = -45 \text{ rad m}^{-2}$ mark the maximum distance to the slab – and therefore to the most remote polarized emission – that can still build up the required Faraday depth when integrating out to 20 kpc. It is clear that the default models cannot explain the observed gap. It is necessary to either invoke a special area just beyond the most distant emission with strongly deviating electron densities and/or

magnetic fields, or an increase in the large scale field strength or electron density, possibly combined with a decrease in pitch angle. In any case it is difficult to defend a distance of more than 1 kpc to the near side of the Faraday rotating area, hence it is likely that the high- ϕ polarized emission is located well within 1 kpc from the Sun. I consider the order of the structures in Fig. 10 accurate. The uncertainties in the distances to individual objects are of order a factor of two for each of the objects.

6. Concluding remarks

I have shown that the polarized Galactic radio synchrotron foreground near $l \approx 150^\circ$, $b \approx -13^\circ$ is very complex. Most lines of sight show radio emitting screens at multiple Faraday depths between -50 and $+100 \text{ rad m}^{-2}$. Because of the layer of negative Faraday depth behind the high- ϕ emission in this part of the sky, it is very difficult to distinguish between Galactic and cluster related polarized emission.

Although the “lens” could very well be associated with the “front”, it remains a peculiar structure. If the “lens” is related to the Perseus cluster, it is not unlike the giant curved relic sources in Abell 3667 (Röttgering et al. 1997) and Abell 2744 (Orru’ et al. 2007). However, it is uncertain how many are still highly polarized at 350 MHz. Although the Abell 2256 relic is highly polarized at 1.4 GHz (Clarke & Enßlin 2006), WSRT observations at 350 MHz (Brentjens 2008) showed it is completely depolarized due to internal Faraday dispersion (Burn 1966). Nor was there evidence for other polarized emission in or near Abell 2256 at 350 MHz. Abell 2255 is another cluster with large, shock related radio filaments at its outskirts (Govoni et al. 2005; Pizzo et al. 2010). Although these sources are highly polarized at 1.4 GHz, they are fully depolarized at 350 MHz and 150 MHz (Pizzo et al. 2010).

The arguments presented in the previous Section and the absence of polarized relic emission at low frequencies in two other clusters with clear evidence for merger shocks at high frequencies leads to the conclusion that all polarized diffuse emission described in de Bruyn & Brentjens (2005) and in this work is Galactic and resides within a few hundred parsecs from the Sun.

Acknowledgements. The Westerbork Synthesis Radio Telescope is operated by ASTRON (Netherlands Foundation for Research in Astronomy) with support from The Netherlands Foundation for Scientific Research (NWO). The Wisconsin H-Alpha Mapper is funded by the National Science Foundation. I thank A. G. de Bruyn for discussions and suggestions.

References

- Baars, J. W. M., & Hooghoudt, B. G. 1974, *A&A*, 31, 323
- Baars, J. W. M., Genzel, R., Pauliny-Toth, I. I. K., & Witzel, A. 1977, *A&A*, 61, 99
- Binney, J., & Dehnen, W. 1997, *MNRAS*, 287, L5
- Brüggen, M. 2003, *ApJ*, 592, 839
- Brentjens, M. A. 2008, *A&A*, 489, 69
- Brentjens, M. A., & de Bruyn, A. G. 2005, *A&A*, 441, 1217
- Burn, B. J. 1966, *MNRAS*, 133, 67
- Cane, H. V. 1979, *MNRAS*, 189, 465
- Clarke, T. E., & Enßlin, T. A. 2006, *AJ*, 131, 2900
- Clarke, T. E., Blanton, E. L., & Sarazin, C. L. 2004, *ApJ*, 616, 178
- Cordes, J. M., & Lazio, T. J. W. 2002, [arXiv:astro-ph/0207156]
- de Bruyn, A. G. 1996, in *The Westerbork Observatory, Continuing Adventure* ed. E. Raimond, & R. Genee, *ASSL*, 207, 109
- de Bruyn, A. G., & Brentjens, M. A. 2005, *A&A*, 441, 931
- Enßlin, T. A., & Gopal-Krishna. 2001, *A&A*, 366, 26
- Enßlin, T. A., & Brüggen, M. 2002, *MNRAS*, 331, 1011
- Enßlin, T. A., Biermann, P. L., Klein, U., & Kohle, S. 1998, *A&A*, 332, 395
- Fabian, A. C., Sanders, J. S., Allen, S. W., et al. 2003, *MNRAS*, 344, L43
- Fletcher, A., & Shukurov, A. 2006, *MNRAS*, 371, L21

- Gómez, G. C., Benjamin, R. A., & Cox, D. P. 2001, *AJ*, 122, 908
- Gaensler, B. M., Madsen, G. J., Chatterjee, S., & Mao, S. A. 2008, *Publications of the Astronomical Society of Australia*, 25, 184
- Govoni, F., Feretti, L., Giovannini, G., et al. 2001, *A&A*, 376, 803
- Govoni, F., Murgia, M., Feretti, L., et al. 2005, *A&A*, 430, L5
- Haffner, L. M., Reynolds, R. J., Tufte, S. L., et al. 2003, *ApJS*, 149, 405
- Han, J. L., & Qiao, G. J. 1994, *A&A*, 288, 759
- Harris, F. J. 1978, in *Proc. IEEE*, 66, 51
- Haslam, C. G. T., Salter, C. J., Stoffel, H., & Wilson, W. E. 1982, *A&AS*, 47, 1
- Haverkorn, M., Katgert, P., & de Bruyn, A. G. 2000, *A&A*, 356, L13
- Haverkorn, M., Katgert, P., & de Bruyn, A. G. 2003a, *A&A*, 403, 1031
- Haverkorn, M., Katgert, P., & de Bruyn, A. G. 2003b, *A&A*, 404, 233
- Heald, G., Braun, R., & Edmonds, R. 2009, *A&A*, 503, 409
- Högbom, J. A. 1974, *A&AS*, 15, 417
- Le Roux, E. 1961, *Annales d'Astrophysique*, 24, 71
- McMullin, J. P., Golap, K., & Myers, S. T. 2004, in *Astronomical Data Analysis Software and Systems (ADASS) XIII*, ASP Conf. Ser., 314, 468
- Merrifield, M. R. 1992, *AJ*, 103, 1552
- Neugebauer, G., Habing, H. J., van Duinen, R., et al. 1984, *ApJ*, 278, L1
- Orrù, E., Murgia, M., Feretti, L., et al. 2007, *A&A*, 467, 943
- Pearson, T. J., & Readhead, A. C. S. 1984, *ARA&A*, 22, 97
- Perley, R. A., & Taylor, G. B. 1999, *VLA Calibrator Manual*, Tech. Rep., NRAO
- Pizzo, R. F., de Bruyn, A. G., Bernardi, G., & Brentjens, M. A., *A&A*, 525, A104
- Platania, P., Bensadoun, M., Bersanelli, M., et al. 1998, *ApJ*, 505, 473
- Reich, P., & Reich, W. 1988a, *A&AS*, 74, 7
- Reich, P., & Reich, W. 1988b, *A&A*, 196, 211
- Röttgering, H. J. A., Wieringa, M. H., Hunstead, R. W., & Ekers, R. D. 1997, *MNRAS*, 290, 577
- Rybicki, G. B., & Lightman, A. P. 1979, *Radiative Processes in Astrophysics* (John Wiley & Sons)
- Sault, R. J., Hamaker, J. P., & Bregman, J. D. 1996, *A&AS*, 117, 149
- Schnitzeler, D. H. F. M., Katgert, P., Haverkorn, M., & de Bruyn, A. G. 2007, *A&A*, 461, 963
- Sokoloff, D. D., Bykov, A. A., Shukurov, A., et al. 1998, *MNRAS*, 299, 189
- Spergel, D. N., Verde, L., Peiris, H. V., et al. 2003, *ApJS*, 148, 175
- Struble, M. F., & Rood, H. J. 1999, *ApJS*, 125, 35
- Sun, X. H., Reich, W., Waelkens, A., & Enßlin, T. A. 2008, *A&A*, 477, 573
- Tan, G. H. 1991, in *Radio Interferometry, Theory, Techniques, and Applications*, ed. T. J. Cornwell, & R. A. Perley, IAU Colloq, 131 ASP Conf. Ser., 19, 42
- Taylor, A. R., Stil, J. M., & Sunstrum, C. 2009, *ApJ*, 702, 1230
- Thompson, A. R., Moran, J. M., & Swenson, Jr., G. W. 1998, *Interferometry and synthesis in radio astronomy* (Malabar, Florida: Krieger Publishing Company)
- Tribble, P. C. 1991, *MNRAS*, 250, 726
- Uyaniker, B., Fürst, E., Reich, W., Reich, P., & Wielebinski, R. 1999, *A&AS*, 138, 31
- Vallee, J. P. 1980, *A&A*, 86, 251
- Wardle, J. F. C., & Kronberg, P. P. 1974, *ApJ*, 194, 249
- Wieringa, M. H., de Bruyn, A. G., Jansen, D., Brouw, W. N., & Katgert, P. 1993, *A&A*, 268, 215
- Wolleben, M., Landecker, T. L., Reich, W., & Wielebinski, R. 2006, *A&A*, 448, 411

Appendix A: Figures

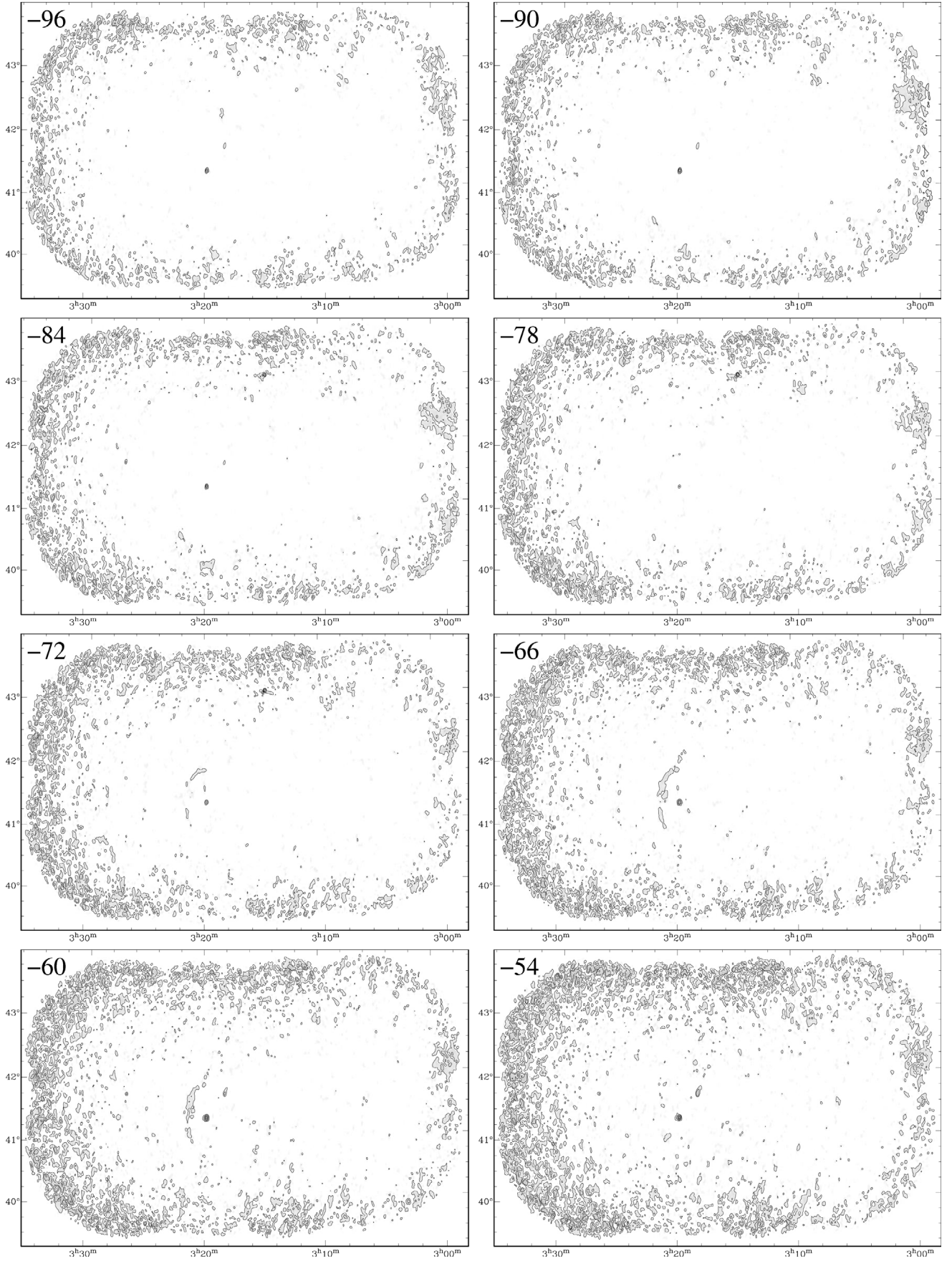


Fig. A.1. Most interesting frames from the RM-cube. The contour levels are 3, 6, 12, 24, ... mJy beam⁻¹ rmtf⁻¹ (1.4, 2.8, 5.5, ... K rmtf⁻¹). The Faraday depth in rad m⁻² is indicated in the top left corner of each frame. The *HPBW* is 2' × 3'.

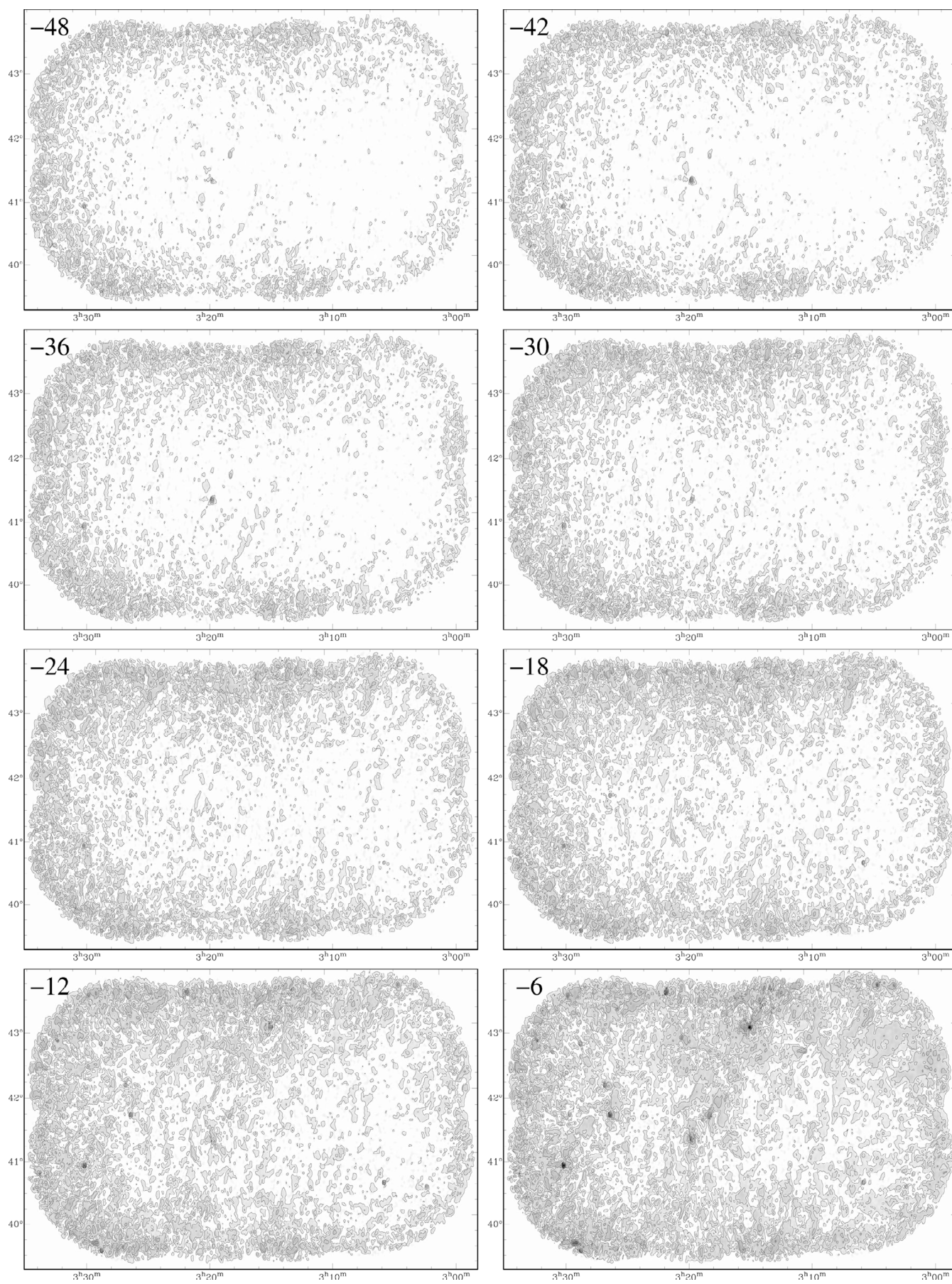


Fig. A.1. continued.

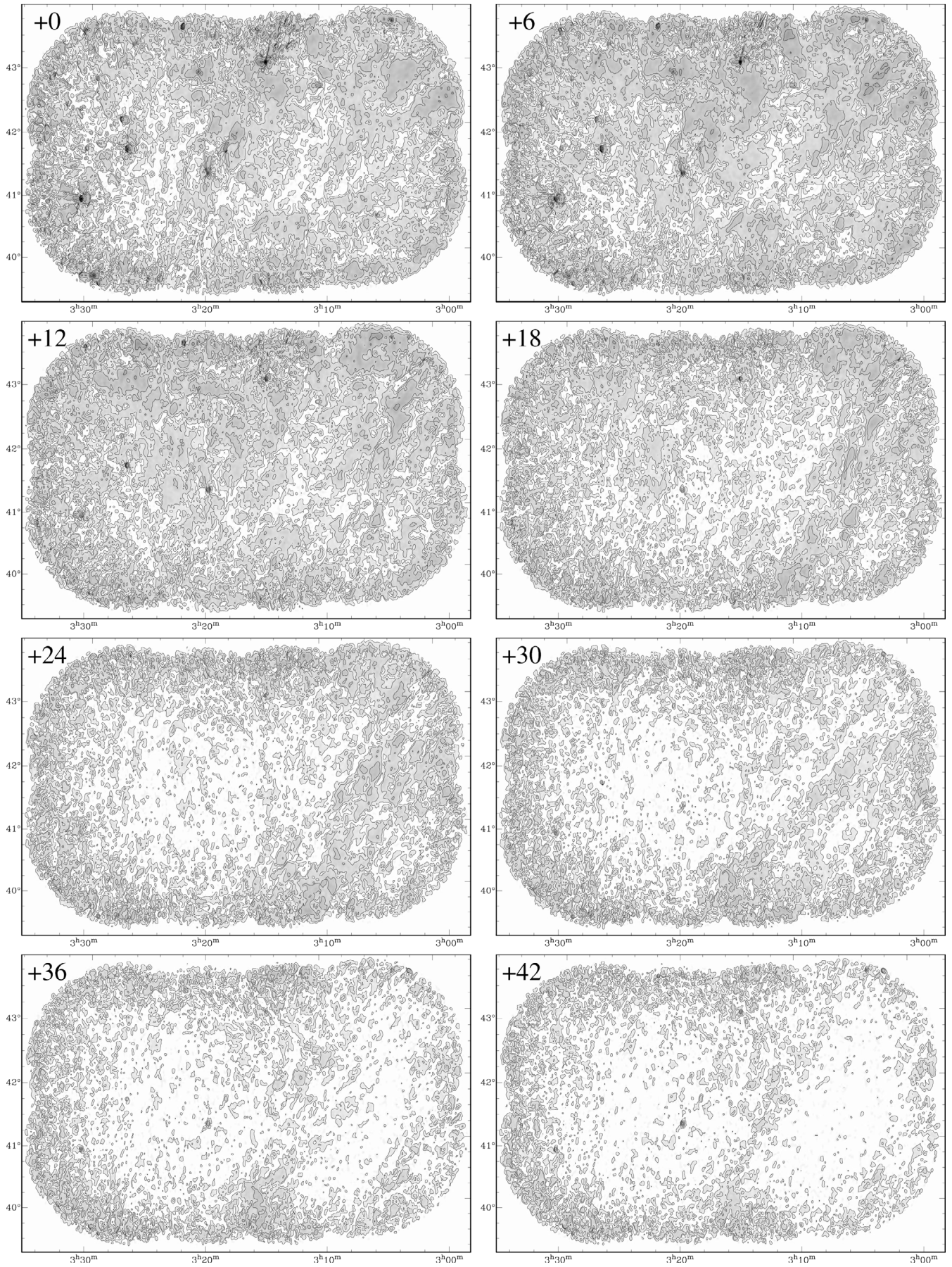


Fig. A.1. continued.

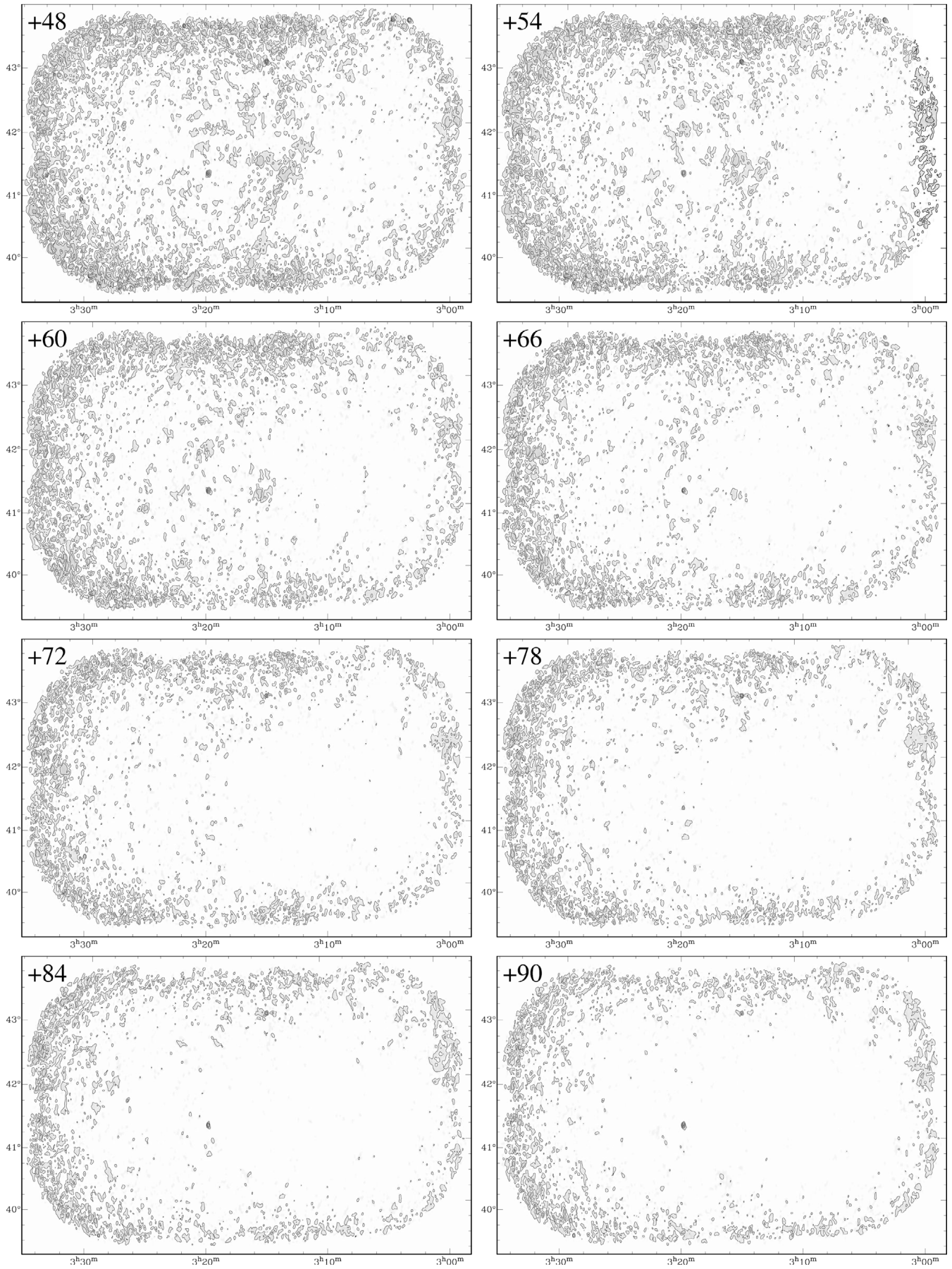


Fig. A.1. continued.

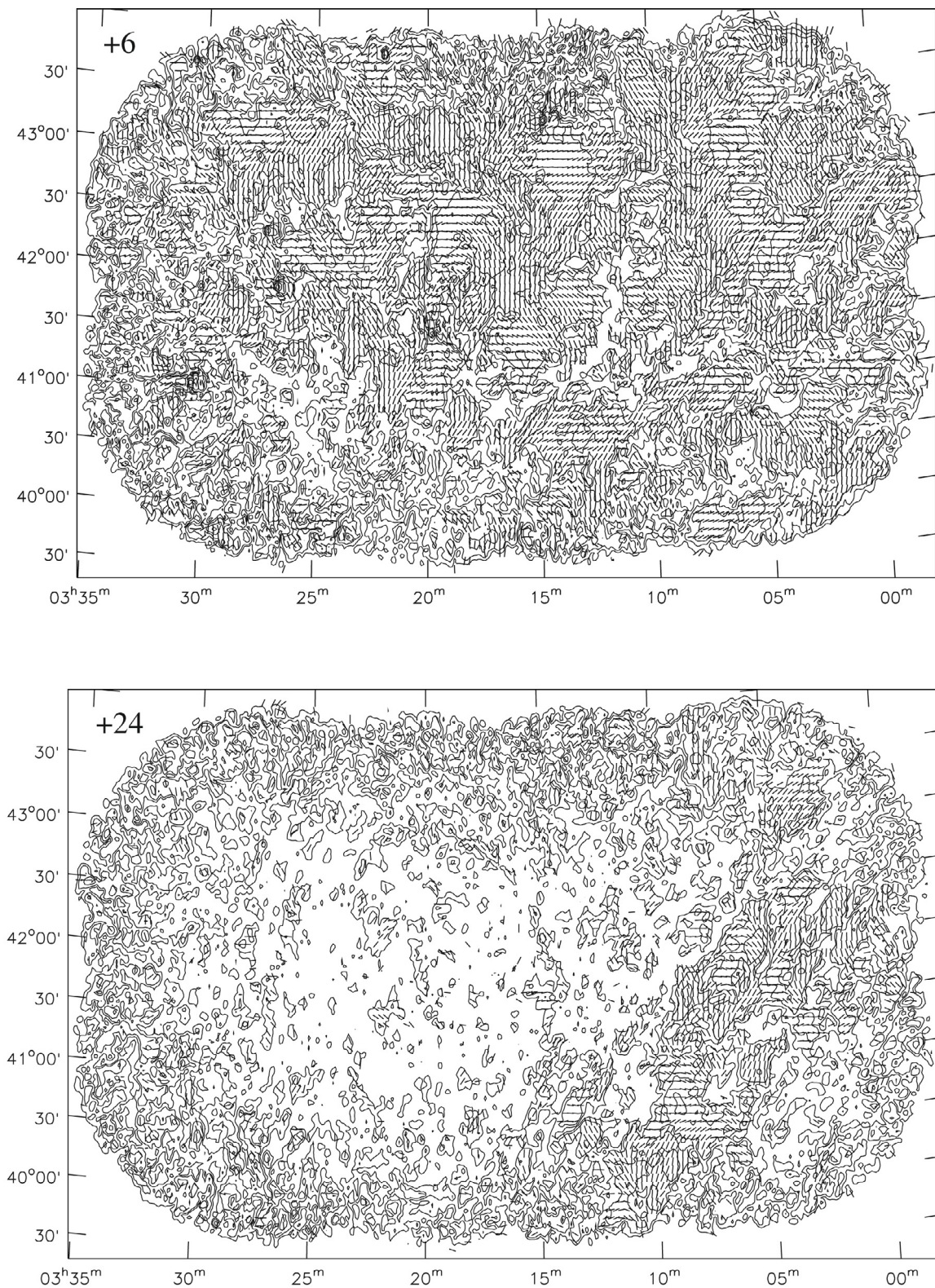


Fig. A.2. Polarization vectors (electric field) at 350.22 MHz overlaid on contour maps of the absolute value of the Faraday dispersion function. Contours are drawn at +3, +6, +12, etc. $\text{mJy beam}^{-1} \text{rmtf}^{-1}$. The polarization vectors are drawn if $|F(\phi)|$ is larger than 5 times the local observed RMS at $|\phi| > 100 \text{ rad m}^{-2}$. The Faraday depth in rad m^{-2} is plotted in the top left corner of each image.

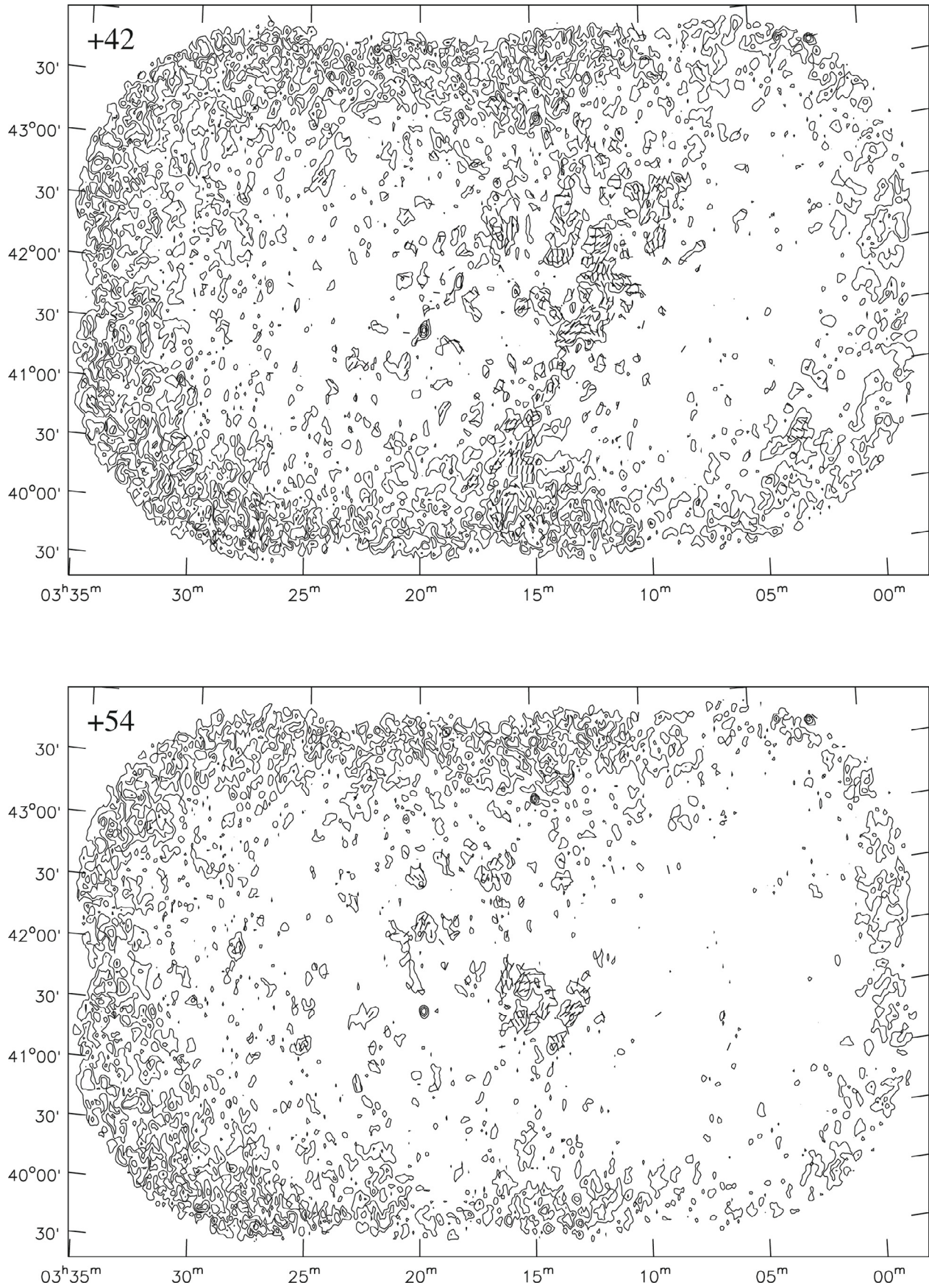


Fig. A.2. continued.